nature neuroscience

ARTICLES

https://doi.org/10.1038/s41593-018-0213-2

Direct vascular channels connect skull bone marrow and the brain surface enabling myeloid cell migration

Fanny Herisson[1], Vanessa Frodermann[1], Gabriel Courties[1], David Rohde[1], Yuan Sun[1], Katrien Vandoorne[1], Gregory R. Wojtkiewicz[1], Gustavo Santos Masson[1], Claudio Vinegoni[1], Jiwon Kim[2], Dong-Eog Kim[2], Ralph Weissleder[1,3], Filip K. Swirski[1], Michael A. Moskowitz[4] and Matthias Nahrendorf[1,5]*

Innate immune cells recruited to inflammatory sites have short life spans and originate from the marrow, which is distributed throughout the long and flat bones. While bone marrow production and release of leukocyte increases after stroke, it is currently unknown whether its activity rises homogeneously throughout the entire hematopoietic system. To address this question, we employed spectrally resolved in vivo cell labeling in the murine skull and tibia. We show that in murine models of stroke and aseptic meningitis, skull bone marrow-derived neutrophils are more likely to migrate to the adjacent brain tissue than cells that reside in the tibia. Confocal microscopy of the skull–dura interface revealed myeloid cell migration through microscopic vascular channels crossing the inner skull cortex. These observations point to a direct local interaction between the brain and the skull bone marrow through the meninges.

Inflammation is an essential defense and repair mechanism that is tightly orchestrated in many human diseases. The hematopoietic system supplies most cellular components of sterile inflammation. The abundance of circulating innate immune cells correlates closely with mortality[1] and fluctuates dramatically after ischemic injury or systemic infection[2–5]. Once recruited to sites of inflammation, neutrophils and other immune cells may defend against infection, but they also have destructive properties. This often contributes to tissue damage and impaired organ function. Specifically, ischemic brain recruits myeloid cells[2,4,6] after activating the bone marrow via the sympathetic nervous system[7]. Given the short life span of myeloid cells in blood and in inflamed tissues, the marrow's supply of these cells influences systemic and local inflammatory activity. Bone marrow is therefore increasingly becoming an organ of therapeutic interest in inflammatory diseases.

On a microscopic scale, functional marrow heterogeneity is being studied intensively, leading to several emerging niche concepts[8]. Quiescent blood stem cells are thought to reside close to osteoblasts and arterioles, while proliferating hematopoietic progenitors are located near sinusoids, which are also discussed as a site from where leukocytes are released from marrow into systemic circulation[9]. Beyond the distinction between red versus yellow marrow, much less is known about the macroscopic heterogeneity of the bone marrow. On the one hand, this relative paucity of data is unexpected, given that this organ system literally spans from head to toe and that there are many different types of long and flat bones. On the other hand, studying such a large and widespread organ is challenging, given that cellular resolution is often required to understand the marrow's function, in particular cell migration. In vivo sampling in humans relies on bone marrow biopsies, which are limited to one site only, mostly the iliac crest.

To begin addressing the knowledge gap on the marrow's functional heterogeneity, we developed a localized cell-tagging approach to label bone marrow cells residing in the mouse skull and tibia with spectrally resolved membrane dyes that serve as cell trackers. This allowed us to determine the origin of leukocytes that were recruited to inflamed tissues after being labeled in the bone marrow. We found that in ischemic and chemically induced models of acute cerebral inflammation, skull bone marrow contributed more neutrophils than tibial marrow. Using an organ-bath microscopy setup to image the inner surface of the mouse skull, we found that neutrophils take an unexpected 'shortcut': myeloid cells migrate toward the inflamed brain through microscopic channels that cross the inner skull cortex and thus directly connect the skull marrow cavities with the dura.

Results

Spectrally resolved site-specific cell tagging. We began by testing two commercially available cell-permeant fluorescent dyes with different excitation and emission spectra, FITC and APC, for their cell-labeling efficiency. Cells separately incubated with the dyes in vitro demonstrated excellent concentration-dependent labeling, which was readily detected by flow cytometry in the respective APC and FITC channels (Fig. 1a). Selective bone marrow microinjection of 3–10 μL cell tracker was then performed in vivo using a Hamilton

[1]Center for Systems Biology, Department of Imaging, Massachusetts General Hospital and Harvard Medical School, Boston, MA, USA. [2]Molecular Imaging and Neurovascular Research Laboratory, Department of Neurology, Dongguk University College of Medicine, Goyang, South Korea. [3]Department of Systems Biology, Harvard Medical School, Boston, MA, USA. [4]Stroke and Neurovascular Regulation Laboratory, Departments of Radiology and Neurology, Massachusetts General Hospital and Harvard Medical School, Boston, MA, USA. [5]Cardiovascular Research Center, Massachusetts General Hospital and Harvard Medical School, Boston, MA, USA. *e-mail: mnahrendorf@mgh.harvard.edu

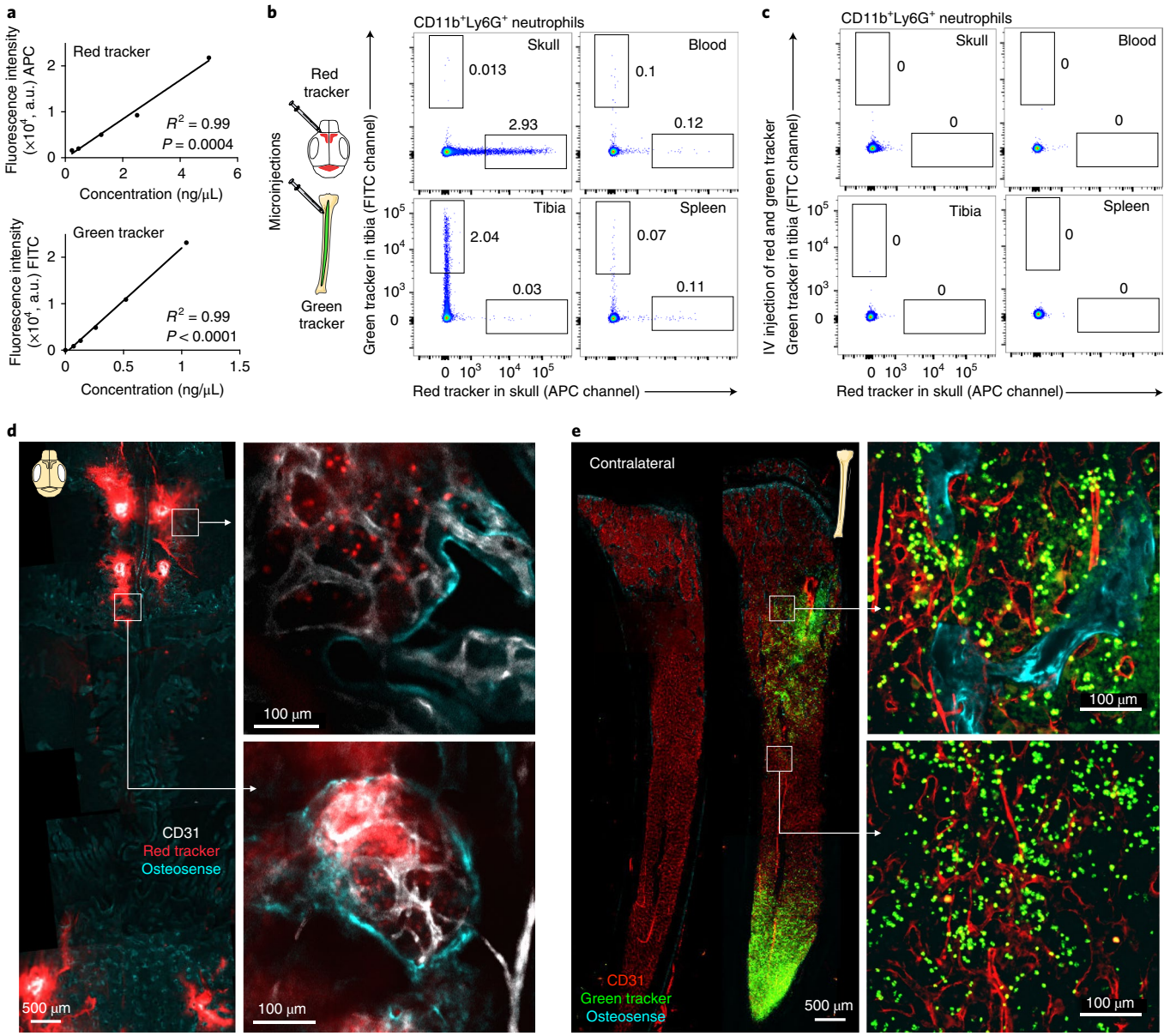

Fig. 1 | Bone marrow cell tagging. a, Concentration-dependent fluorescence intensity of in vitro-labeled bone marrow cells by flow cytometry for the red (APC, $n = 5$ mice) and green (FITC, $n = 6$ mice) cell trackers in two independent experiments. **b**,**c**, Representative flow cytometry from naive mice 24 h after (**b**) marrow microinjection of red and green cell trackers or (**c**) intravenous (IV) injection (independently repeated twice with same results). **d**,**e**, Confocal imaging of (**d**) calvarium and (**e**) tibia after microinjection of red and green cell trackers into 2 mice (single experiment). Bone outline is visualized with Osteosense (turquoise) and endothelium with CD31 in vivo immunolabeling.

syringe equipped with a custom 34-gauge blunt needle. Based on the observed in vitro labeling efficiencies, we chose a cell tracker dose for in situ bone marrow labeling that created a steep fluorescence gradient between the marrow compartment and the systemic circulation. Twenty-four hours after microinjections into the skull and the tibia, we examined the labeling efficiency for neutrophils harvested from the injection and remote control sites, specifically the spleen and blood. We focused on neutrophils because these cells are numerous first responders to tissue injury. Labeled neutrophils were readily detected at sites of injection by flow cytometry (Fig. 1b). Low numbers of labeled cells were also detected in the blood and spleen (Fig. 1b). Cell exposure to locally concentrated dye after injection into the marrow yielded high cell-associated fluorescence intensities (Fig. 1b), whereas intravenously injected dye, which resembles cell-unassociated dye leaking into the circulation after marrow injection, was so diluted that we did not detect any labeled cells (Fig. 1c).

Confocal microscopy of the skull (Fig. 1d) and the tibia (Fig. 1e) following cell tracker injection showed locally contained fluorescence and efficient cell labeling. While dye microinjections slightly decreased cell viability, this occurred to the same extent in both compartments and did not alter marrow cell content or migration of cells to the inflamed brain after stroke (Supplementary Fig. 1a,b). Following skull injections, we used microglia, which are not bone marrow-derived, as 'witness cells' to explore whether skull marrow labeling is locally contained or spills over in inflammatory brain conditions. Microglial cells were only APC⁺ when red cell tracker was purposely injected through the skull below the dura, but not after injection into the marrow (Supplementary Fig. 1c,d). Taken together, these data demonstrate that intramarrow cell-tracker

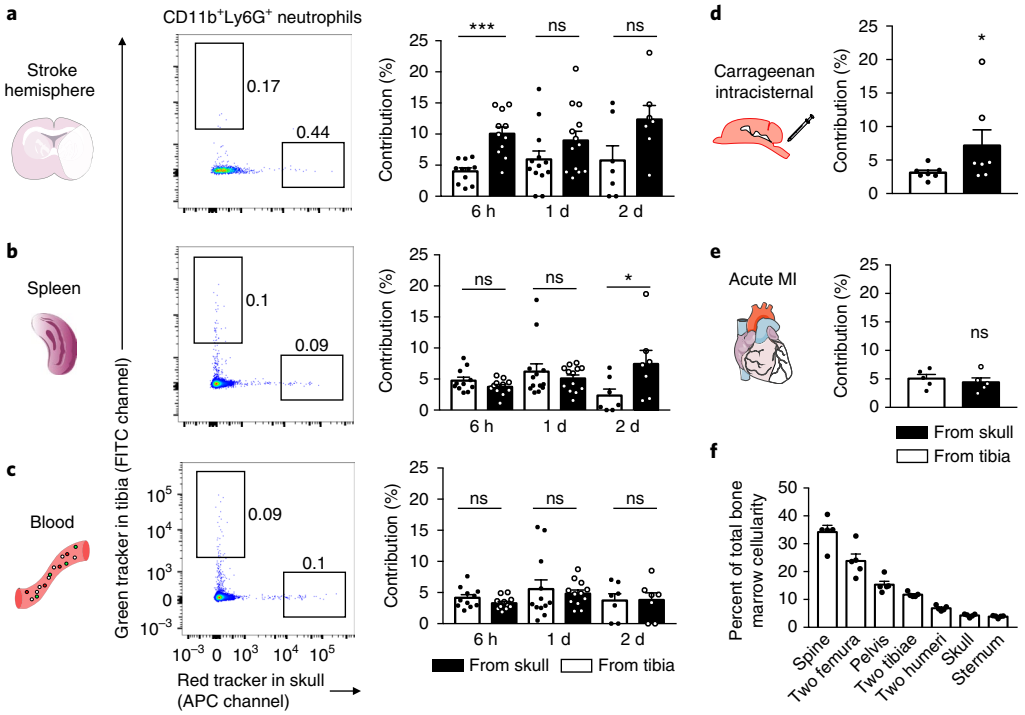

Fig. 2 | Neutrophil tracking in stroke, carrageenan-induced meningoencephalitis and myocardial infarction. a–c, Representative examples of neutrophil tracking after tagging in skull (red) and one tibia (green tracker) in the same animal: (**a**) in the ischemic brain, (**b**) the spleen, and (**c**) blood after stroke induced by permanent occlusion (6 h, $n=11$ mice; 5 experiments; 1 d, $n=13$ mice for brain and spleen, $n=12$ mice for blood; 5 experiments; 2 d, $n=7$ mice; 2 experiments). Contributions were normalized to cell frequency at injection site (two-tailed paired Wilcoxon test; brain: 6 h, $^{***}P=0.002$; 1 d, $P=0.127$; 2 d, $P=0.219$; spleen: 6 h, $P=0.206$; 1 d, $P=0.787$, 2 d, $^{*}P=0.016$; blood: 6 h, $P=0.153$; 1 d, $P=0.97$, 2 d, $P=0.812$). **d**,**e**, Neutrophil exit from the skull and the tibia (**d**) in aseptic meningoencephalitis ($n=7$ mice; 4 experiments, two-tailed paired Wilcoxon test, $^{*}P=0.031$) and (**e**) after myocardial infarction ($n=5$ mice; 1 experiment, two-tailed Wilcoxon test, $P=0.813$). **f**, Size of bone marrow compartments ($n=5$ mice). Data are mean ± s.e.m.; ns, nonsignificant. See also Supplementary Fig. 2 for gating and Supplementary Fig. 3 for related analyses.

injections label cells in the skull and tibia with an efficiency sufficient for systemic cell tracking by flow cytometry.

Tracking cell origins in different inflammatory sites. We next used the cell-tracking approach to determine relative neutrophil sources in several models of acute inflammation, including ischemic stroke, acute myocardial infarction, and inflammation induced by intracisternal carrageenan injection, which leads to aseptic meningoencephalitis[10] (Fig. 2). To explore neutrophil contributions to inflammatory sites, we first injected red and green cell trackers into the skull and tibia, respectively. Destination tissues were then processed and stained with an antibody cocktail for flow-cytometry detection of cell surface markers, reserving two channels for the spectrally resolved cell trackers. Flow cytometry gates were positioned based on intravenously injected control animals (Supplementary Fig. 2). We focused on neutrophil migration during early inflammation and normalized labeled-cell frequencies in tissues of interest to the labeling efficiency at the site of origin (Fig. 2a–e). We found that the skull contributed significantly more neutrophils to the ischemic brain hemisphere than the tibia (Fig. 2a). The frequency of cells originating from the skull or the tibia was not significantly different in the spleen and the blood, with the exception of the spleen 2 d after stroke, which showed a decreased contribution of cells from the tibia (Fig. 2b,c). Raw frequencies and ratios to blood are provided in Supplementary Fig. 3. Like ischemic stroke, intracisternal injection of carrageenan, leading to meningoencephalitis[10], also elicited a higher contribution of skull neutrophils to brain inflammation (Fig. 2d). In contrast, 1 d after myocardial infarction, the neutrophil contributions of the skull and the tibia, which are both distant from the heart, were comparable (Fig. 2e), indicating that the proximity of brain inflammation to skull bone marrow may influence cell migration paths. We next used ex vivo confocal microscopy of the fresh brain after in vivo staining of the vasculature to explore the location of cells tagged in skull or tibia after induction of meningoencephalitis. We primarily found cells originating from the skull (8 of 12 tagged cells), which were located in the brain parenchyma, outside of the vasculature (Supplementary Fig. 4). The observation of preferential skull neutrophil recruitment to the brain was not caused by the size of the labeled marrow compartment, as the cellularity of one tibia roughly equaled that of the skull (Fig. 2f).

Myeloid cell population dynamics depend on marrow location. To explore whether the observed migration heterogeneity causes differences in the marrow's myeloid cell numbers, we enumerated neutrophils and monocytes in the skull and tibia at different timepoints after stroke. Compared to sham controls, stroke led to a significant decrease of neutrophils and monocytes in the skull bone marrow 6 h after ischemia (Fig. 3a,b), which reflected the release of myeloid cells after brain injury. Notably, in the tibia, the cell number did not decrease significantly (Fig. 3a,c). Likewise, the vertebral marrow did not show a major reduction of myeloid cells 6 h after stroke (Supplementary Fig. 5). When normalized to sham controls, the poststroke skull marrow contained significantly fewer neutrophils and monocytes than the tibia (Fig. 3d,e). Viewed together with the higher cell traffic from the skull (Fig. 2a), these data indicate that after stroke, the skull marrow released myeloid cells more vigorously than the tibia. Comparing naive skull and tibial neutrophils in vitro, we found no difference in the cells' migration through activated brain endothelium (Supplementary Fig. 6).

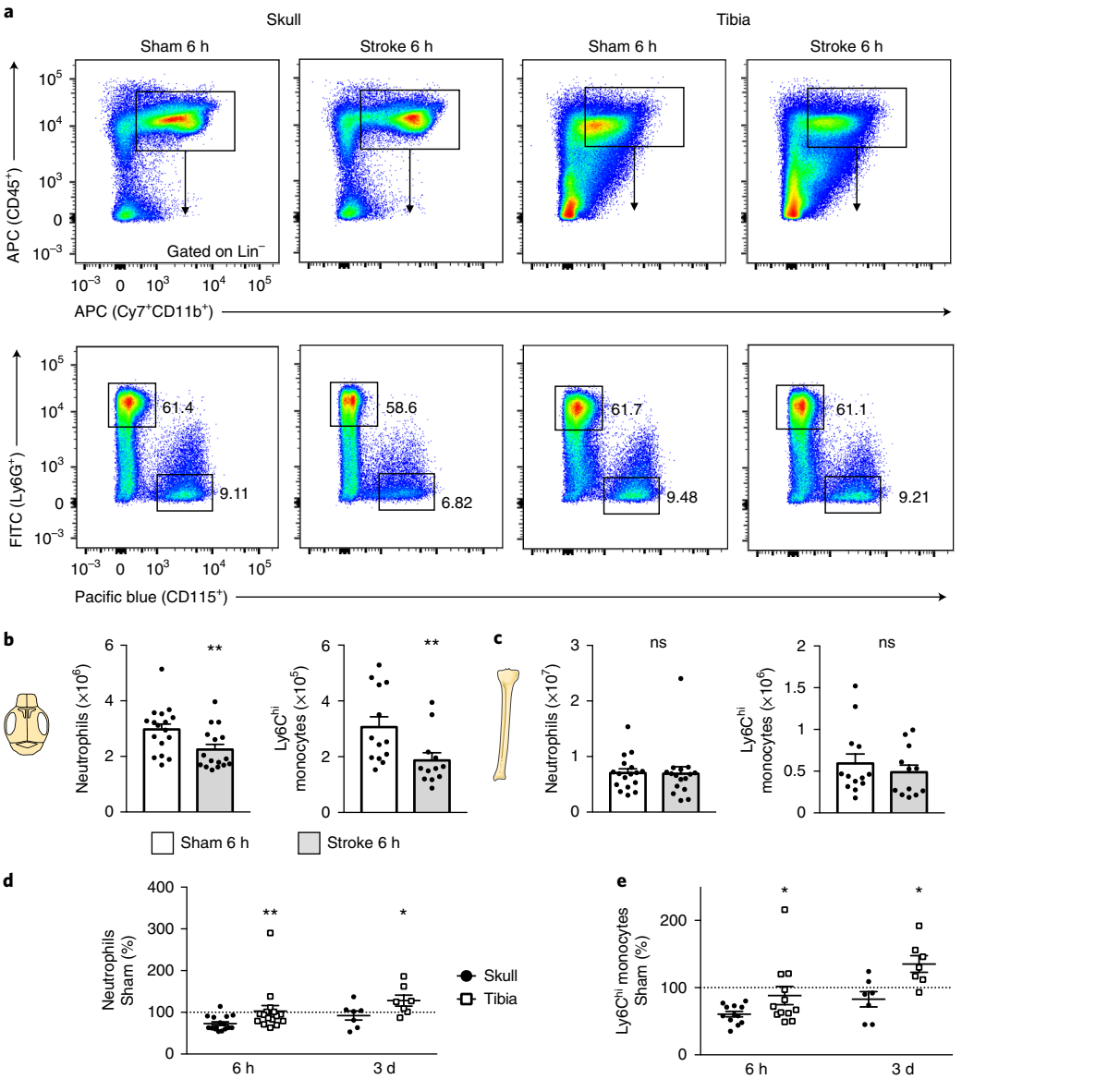

Fig. 3 | Skull releases more inflammatory cells after stroke. a, Representative flow cytometry plots of skull and tibia bone marrow 6 h after stroke induced by 30 min middle cerebral artery occlusion (MCAO) or sham controls (6 experiments). Additional gating is shown in Supplementary Fig. 2. **b**, Neutrophil and monocyte numbers in skull after stroke or sham controls (neutrophils: $n=16$ mice for stroke, $n=17$ mice for sham, 6 experiments; Ly6C^{hi} monocytes, $n=13$ mice for stroke, $n=12$ mice for sham, 4 experiments; two-tailed Mann–Whitney test, neutrophils, $^{**}P=0.008$; monocytes, $^{**}P=0.007$). **c**, Neutrophil and monocyte numbers in both tibiae (neutrophils, $n=16$ mice for stroke, $n=17$ mice for sham, 6 experiments; Ly6C^{hi} monocytes, $n=13$ mice for stroke, $n=12$ mice for sham, 4 experiments; two-tailed Mann–Whitney test, neutrophils, $P=0.49$; monocytes, $P=0.54$). **d**,**e**, Data normalized to sham at 6 h (neutrophils, $n=16$ mice per condition; monocytes, $n=12$ mice; 4 experiments) and 3 d after stroke ($n=7$ mice per condition, 3 experiments; two-tailed paired Wilcoxon test; neutrophils: 6 h, $^{**}P=0.002$, skull vs. tibia; 3 d, $^{*}P=0.031$, skull vs. tibia; monocytes: 6 h, $^{*}P=0.016$, skull vs. tibia; 3 d, $^{*}P=0.016$, skull vs. tibia). See Supplementary Fig. 5 for spine; ns, nonsignificant.

To begin deciphering the mechanisms behind the observed marrow heterogeneities, we compared SDF-1 levels between the skull and tibial marrow by enzyme-linked immunosorbent assay (ELISA). SDF-1 retains leukocytes in hematopoietic niches, and its decrease leads to monocyte and neutrophil release from the marrow[11]. SDF-1 production increases in the brain after stroke[12]. Six hours after stroke, we observed a significant decline in SDF-1 levels in the skull only (Fig. 4a), which may have contributed to a preferential release of neutrophil from this site. Since bone marrow vascular permeability may regulate leukocyte release, we assessed this parameter using an Evans Blue assay[9]. Six hours after stroke, vascular permeability did not change significantly in either skull or tibia (Fig. 4b,c). A trend toward higher permeability of the skull marrow, after cisternal carrageenan injection, and a decrease in tibial marrow permeability were observed (Fig. 4d). Thus, regional heterogeneities in the leukocyte retention factor SDF-1 and vascular permeability may contribute to the preferred mobilization of skull neutrophils in the context of brain inflammation.

Direct vascular channels connect skull marrow and the CNS surface. Since the skull provides more neutrophils to acutely inflamed brain tissue than remote tibial marrow, we tested the hypothesis that this is due to the proximity of the skull marrow to the brain. We reasoned that direct vascular connections could provide either a conduit

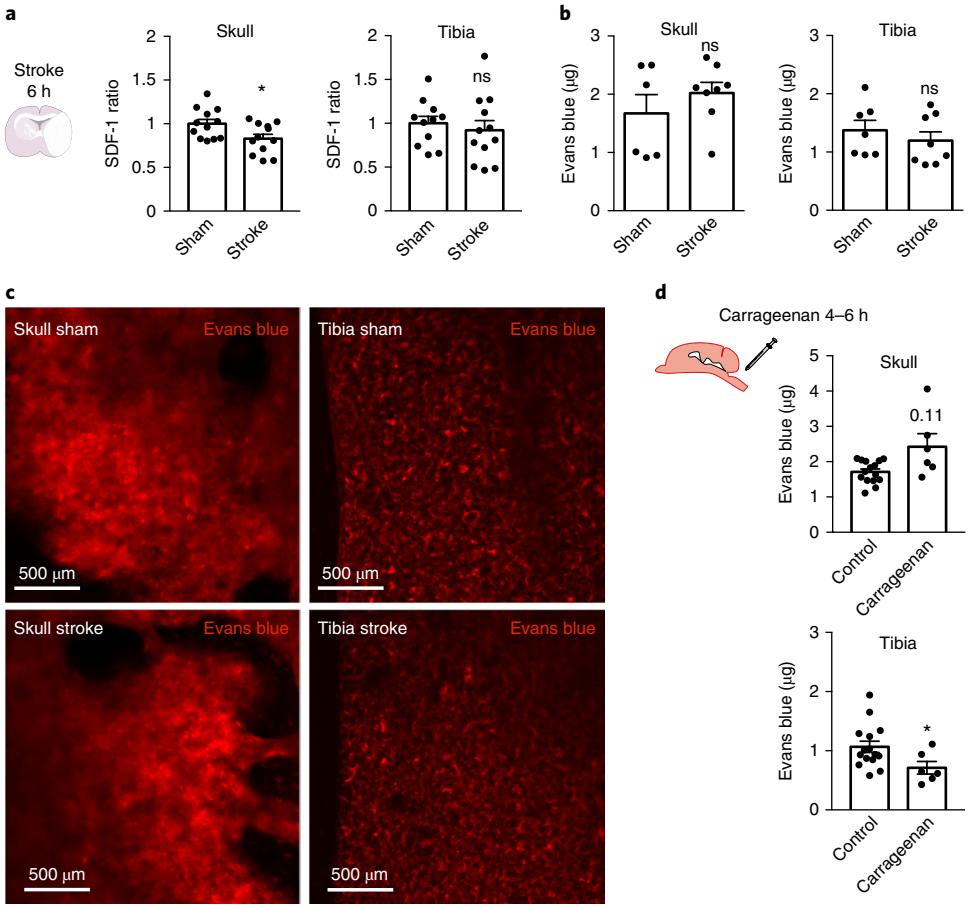

Fig. 4 | Retention factor SDF-1 and bone marrow permeability. a, SDF-1 protein ELISA in skull and tibia bone marrow 6 h after stroke induced by 30-min occlusion. Data are from 2 separate experiments and normalized to the mean sham value (stroke, $n=12$ mice for skull, $n=12$ mice for tibia; sham, $n=12$ mice for skull, $n=11$ mice for tibia sham; two-tailed Welch's t test; skull, $^*P=0.025$; tibia, $P=0.567$). **b**, Evans Blue permeability after stroke induced by 30-min occlusion ($n=6$ mice for sham, $n=8$ mice for stroke, 5 experiments; two-tailed Mann–Whitney test; skull, $P=0.59$; tibia, $P=0.28$). **c**, Histology of Evans Blue in skull and tibia bone marrow after stroke and in sham animals. **d**, Evans Blue permeability after carrageenan injection (control, $n=15$ mice; carrageenan, $n=6$ mice, 6 experiments; two-tailed Welch's t test; skull, $P=0.112$; tibia, $^*P=0.027$). Data are mean ± s.e.m.; ns, nonsignificant.

for danger signals that alert the skull marrow of CNS inflammation or a path for leukocytes that migrate toward the brain. When studying the skull–brain intersection by confocal microcopy on coronal views, we observed a number of channels that connect marrow cavities with the dura mater through the skull's inner cortex (Fig. 5). The channels were surrounded by Osteosense signal (Fig. 5a), which arose from osteoblasts lining the bone surface[13]. Inside these channels, we detected fluorescent signal for CD31, indicating endothelial lining, Cx3cr1^{GFP}-positive monocytes and Ly6G$^+$ neutrophils (Fig. 5a–c). To image the inside of the skull's surface, we immersed freshly harvested skull in an organ bath, with the interior surface facing the microscope's objective (Fig. 5b). In this orientation, we likewise observed numerous channels traversing the inner cortical layer of the skull bone. This experimental setup provided the opportunity to acquire z-stacks and time-lapse data (Fig. 5d,e). Notably, we frequently observed Ly6G$^+$ neutrophils migrating through channels, ultimately emerging at the inner skull surface (Supplementary Video 1). To determine whether there is cell traffic in these channels in vivo, we next imaged 4-week-old mice. Young mice have thinner skulls, which allowed us to image the inner skull bone layers in vivo. In these mice, we observed that blood flow through channels was directed toward the marrow cavities. However, neutrophils traveled against the flow, toward the dura mater, after induction of stroke (Fig. 5f and Supplementary Videos 2 and 3). Neutrophils exited channels more frequently in skulls harvested from mice with brain inflammation after stroke or intracisternal carrageenan injection (Fig. 6a–c and Supplementary Videos 4 and 5).

In adult mice, the channels were 21.6 ± 0.9 µm in diameter (Fig. 6d). Electron microscopy confirmed the channels' endothelial lining and showed that the channel lumen connects with vasculature in the dura mater (Fig. 7a–d). After stroke, neutrophils exited blood vessels in the dura (Supplementary Fig. 7). High resolution ex vivo X-ray computed tomography (microCT) revealed the channels' wide distribution throughout the inner and outer murine skull cortices (Fig. 8a–e and Supplementary Video 6). Measured by microCT, the channels were similar in size in the inner and outer skull cortex (Fig. 8f). Compared to the histology data, the average channel diameter was slightly lower on microCT, which we attribute to partial volume effects and the lower resolution of the X-ray based modality. In the tibia, we observed similar channels traversing the bone cortex (Fig. 8f).

Finally, we explored whether such channels exist in humans. To this end, we imaged craniectomy specimens obtained during decompression surgery in 3 patients (clinical information is provided in the Methods). In all three samples, we identified similar channels (albeit with 5.3-fold larger mean diameters) connecting the inner skull cortex surface with marrow cavities (Fig. 8g–k). In contrast to mice, channels through the human outer skull cortex

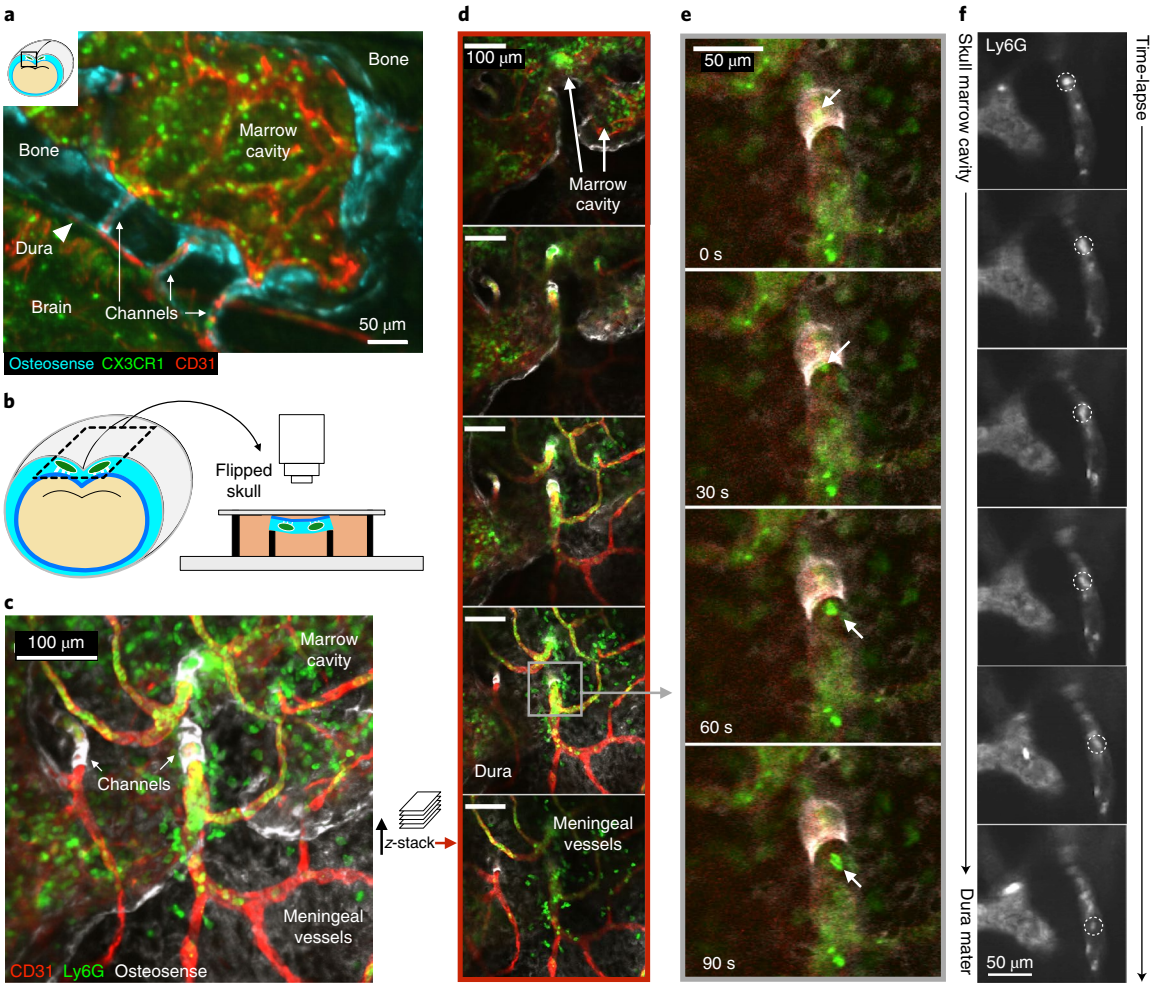

Fig. 5 | Ex vivo confocal microscopy of channels connecting the skull marrow to the dura. a, Coronal view of the skull and brain in a Cx3cr1^{GFP} mouse showing channels in relation to the brain, bone, and dura (single experiment). **b**, Ex vivo skull marrow bath using *N*-Formylmethionyl-leucyl-phenylalanine (FMLP)-containing medium. **c**,**d**, Representative images of (**c**) collapsed *z*-stack and (**d**) single slices after intracisternal carrageenan injection. **e**, Time series of neutrophil channel exit (replicated four times). See also Supplementary Video 1. **f**, In vivo time-lapse of neutrophil migrating through a channel, representative example of imaging in 2 mice after stroke (permanent MCAO). See also Supplementary Videos 2 and 3.

were larger than channels traversing the inner skull cortex (Fig. 8l). In the interior human skull cortex, the channels occupied 2.5 ± 0.2% of the bone volume.

Discussion

We here apply a method for tracking cell origins from different bone marrow locations to study inflammation in several organs. When inflammation occurred in the brain, the organ had a high propensity to recruit neutrophils from skull bone marrow. We detected this recruitment bias by flow cytometry after tagging cells in the marrow. No such preference was present when inflammation befell the heart, suggesting that anatomic proximity could be instrumental for leukocyte migration in general and specifically for inflammatory brain disorders. Confocal microscopy on the inside of the skull after stroke or intracisternal carrageenan injection revealed myeloid cell traffic through small vascular channels that connect the skull marrow with the meninges. These data challenge the current dogma that after any inflammatory stimulus, the marrow homogeneously releases leukocytes into the systemic circulation, followed by cell recruitment into the injured site from the blood pool.

The meninges carry a rich vascular network that originates from the cerebral arteries, external carotid arteries, and the diploic veins. Diploic veins connect the pericranial and endocranial venous system through the skull[14,15]. On the brain surface, meningeal vessels can expand through the arachnoid layer, which provides access to the cerebrospinal fluid[14]. Diploic vessels pass through the human cranium mostly in the parietal bone[16]. Those vessels average 1.5 mm in diameter, but diploic veins also connect to a microscopic network of venous channels[14,17]. Specifically, human corrosion casts display numerous microvessels branching toward the marrow cavity[14]. Our microCT data indicate that there are direct connections between skull marrow cavities and the inner surface of the skull bone in mice and humans. Whether leukocytes frequent these channels in humans, in parallel to our in vivo microscopy observations in mice, is currently unclear.

In the setting of brain inflammation, vascular structures may be damaged or become leaky. Such pathologies, our data indicate, could trigger direct skull marrow supply of inflammatory cells to the surface of the brain. After stroke, we observed leukocytes moving through channels against the blood flow toward the dura, as well as extravasated neutrophils in the dura, which supports the idea that skull-derived neutrophils may migrate directly to the brain. Other cell types or pathogens may travel the same way. Notably, meninges emerge as a site of early inflammatory

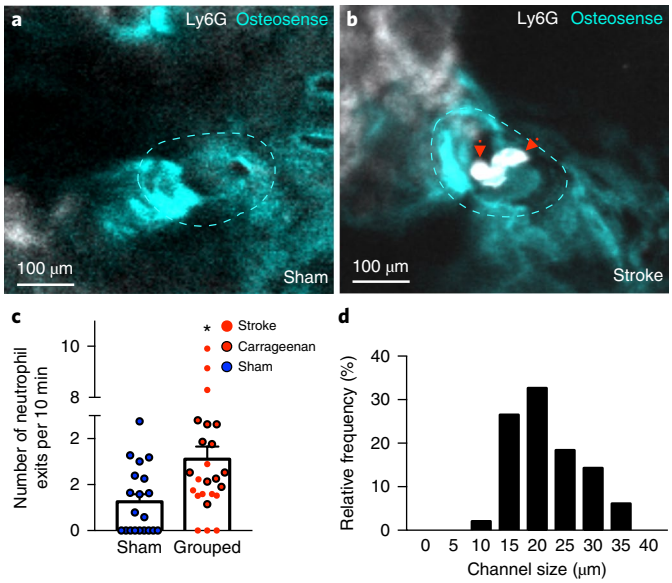

Fig. 6 | Cells exit channels in organ bath. a,**b**, Representative examples of channels (dotted line) in (**a**) sham control and (**b**) stroke (permanent MCAO). See also Supplementary Videos 4 and 5. **c**, Number of neutrophil exits, two-tailed Mann–Whitney test; $^{*}P = 0.011$; sham, $n = 20$ channels; acute inflammation, $n = 24$ (including 13 stroke) channels per group; 4 independent experiments; sham, $n = 4$ mice; stroke, $n = 3$ mice; carrageenan, $n = 4$ mice). Data are mean ± s.e.m. **d**, Distribution of channel diameter by histology (sham, $n = 4$ mice; stroke, $n = 3$ mice; carrageenan, $n = 4$ mice).

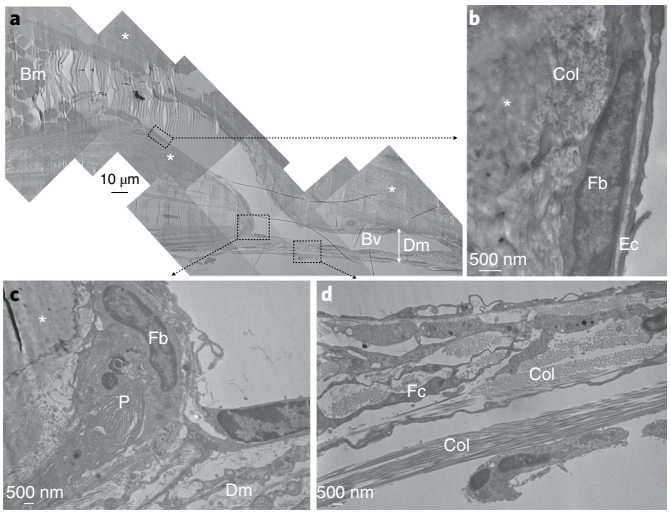

Fig. 7 | Electron microscopy of channel. a, Entire channel connecting a skull bone marrow cavity (bm) filled with blood cells with a blood vessel (bv) in the dura mater (dm) while traversing the inner bone cortex (asterisks); representative image from a single experiment. **b**, Channel is clad with endothelial cells (ec) above fibroblasts (fb). **c**, Connective tissue in the dura mater in the vicinity of the channel, fibroblast, and plasma cell (P). **d**, Dura mater with collagen (col) and fibrocyte (fc).

processes in chronic neurological diseases such as multiple sclerosis[18]. Innate immune cells, particularly neutrophils and monocytes, are also being studied in the setting of Alzheimer's disease[19–21]. Skull neutrophil supply could thus contribute to chronic neurodegenerative disorders like Alzheimer's, as neutrophils are observed at the cerebromeningeal level early in the course of the disease[21]. Trauma to the skull may also impact the dynamics and supply of inflammatory cells to the meninges and the brain, possibly affecting inflammatory activity in the CNS.

Because the channels are not a one-way street, signaling molecules originating from the inflamed brain may preferentially reach the skull marrow. This could trigger local alteration of the hematopoietic stem cell niche, as indicated by our data on SDF-1, and perhaps also condition leukocytes and their progenitors. As a consequence, skull neutrophils may be more inflammatory, more numerous, and more prone to interact with brain macrophages, in particular at the perivascular level[22–24]. Altogether, such local interactions may explain the preferential skull neutrophil recruitment we observed in the inflamed brain and may initiate neuroinflammatory cascades.

Leukocyte access to ischemic brain may rely on alternate migratory paths independent of the systemic circulation, a speculation that agrees with our observation of bias toward skull marrow recruitment in CNS inflammation. We observed leukocytes in perivascular spaces of the dura after stroke induction, similarly to prior findings in rodents and humans that stressed the importance of the leptomeningeal vessels for leukocyte migration into inflamed brain tissue[25,26]. Though this study was limited by the small number of cells available for histological analysis, we still found that skull neutrophils were more numerous at the brain surface than cells originating from the tibia, which suggests that leptomeningeal vessels may enrich for leukocytes originating from the skull marrow.

The dura is composed of thick collagen layers and contains arterial, venous, and lymphatic components[27]. Dural lymphatic vessels may carry immune cells from the CNS to the periphery[28,29]. However, lymphatic drainage is absent from bone marrow, and the channel microanatomy is not suggestive of lymphatic endothelium. Whether leukocytes extravasated in the dura enter the lymphatic system or the brain parenchyma requires further investigation. In steady state, an impervious barrier separates the dura from the leptomeninges[27]. This may change in inflammatory conditions. Direct leukocyte migration through these layers could represent an alternative migratory path, particularly in the context of severe stroke or meningitis that triggers inflammation on the brain's surface. Proteases released from activated mast cells and macrophages in the dura may loosen the extracellular matrix, thus facilitating cell migration[30–32].

Our work focused on early inflammatory events and neutrophil migration, cells considered to be first responders to infection and injury. In the setting of sterile inflammation, neutrophils are destructive, as their defensive weaponry inflicts damage on the organ stroma[33]. In ischemic stroke, and particularly after reperfusion, neutrophils contribute to blood–brain barrier disruption, edema, oxidative stress, protease activity, neuronal death, infarct expansion, and poor neurological outcomes[2,34]. Neutrophils are among the cells with the shortest lifespans; therefore, the study of their production and migration provides insight into mechanisms that bring about the population increase seen in inflamed tissue.

This work poses several questions. The channels' function in humans is currently unknown, but it would be valuable to estimate the contribution of this migratory path in steady state and during chronic and acute brain inflammation. It would be of interest to explore whether and how the blood flow and cell migration through these channels is regulated and how it changes with increased intracranial pressure. An additional putative channel function is information transfer, as soluble inflammatory factors, including danger-associated molecular patterns arising from ischemic brain, may alert the skull marrow[6]. Finally, it will be of interest to study whether inhibition of cell migration through the described channels has anti-inflammatory effects.

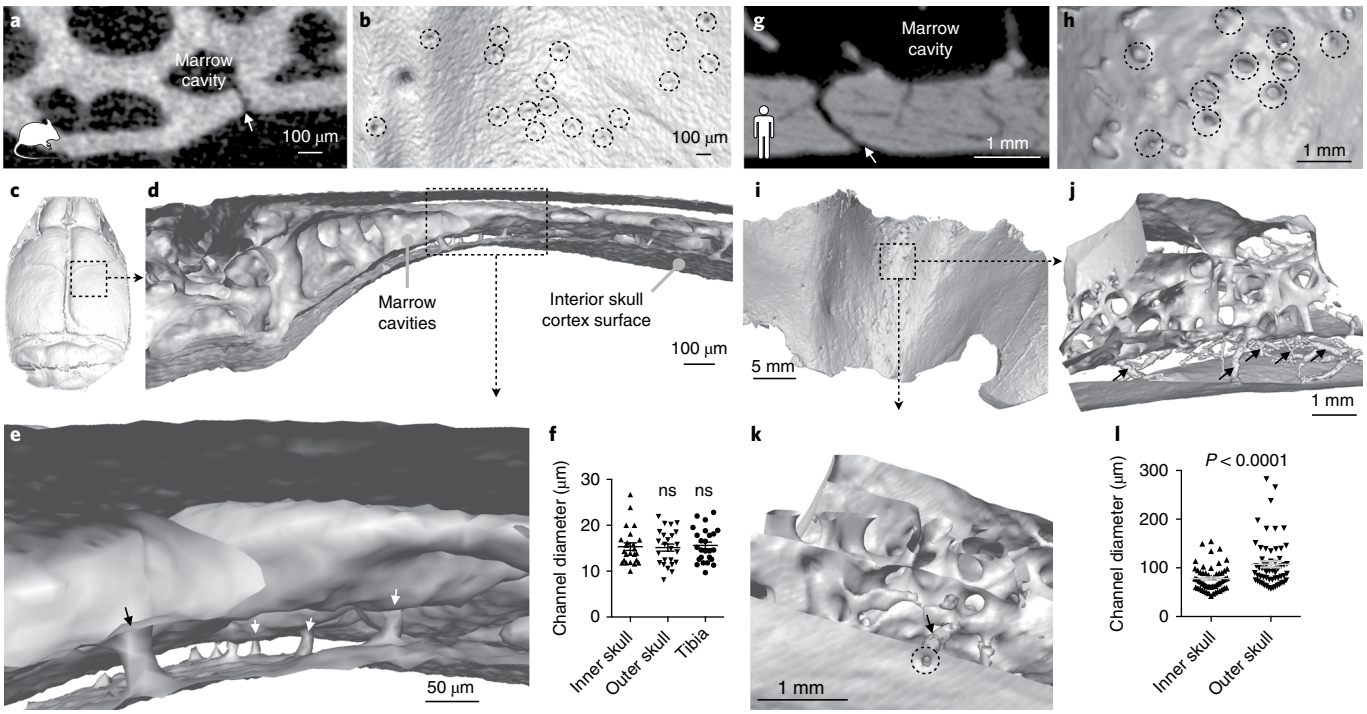

Fig. 8 | Channels in the mouse (a–f) and human (g–l) skull imaged by microCT. a,**g**, Coronal view of channel (arrow) in a mouse (**a**) and human (**g**). **b**,**h**, Interior skull surface reconstruction; channel openings indicated by dashed circles. **c**,**i**, Interior skull surface reconstruction. **d**,**e**,**j**,**k**, Coronal surface rendering of channels (arrows). **f**,**l**, Channel diameter according to location in mouse and in human. Each point is one channel. Data were obtained in 1 mouse (inner and outer skull, $n = 24$ channels; tibia, $n = 25$ channels; one-way ANOVA; $P = 0.96$) and 3 humans (inner and outer skull, $n = 60$ channels; two-tailed t test with Welch's correction; $P < 0.0001$). Data are mean ± s.e.m. See Supplementary Video 6.

Methods

Methods, including statements of data availability and any associated accession codes and references, are available at https://doi.org/10.1038/s41565-018-0195-y.

Received: 24 July 2017; Accepted: 23 July 2018;
Published online: 27 August 2018

References

1. Swirski, F. K. & Nahrendorf, M. Leukocyte behavior in atherosclerosis, myocardial infarction, and heart failure. *Science* **339**, 161–166 (2013).
2. Jickling, G. C. et al. Targeting neutrophils in ischemic stroke: translational insights from experimental studies. *J. Cereb. Blood Flow Metab.* **35**, 888–901 (2015).
3. Kamel, H. & Iadecola, C. Brain-immune interactions and ischemic stroke: clinical implications. *Arch. Neurol.* **69**, 576–581 (2012).
4. Offner, H. et al. Experimental stroke induces massive, rapid activation of the peripheral immune system. *J. Cereb. Blood Flow Metab.* **26**, 654–665 (2006).
5. Courties, G., Moskowitz, M. A. & Nahrendorf, M. The innate immune system after ischemic injury: lessons to be learned from the heart and brain. *JAMA Neurol.* **71**, 233–236 (2014).
6. Gelderblom, M., Sobey, C. G., Kleinschnitz, C. & Magnus, T. Danger signals in stroke. *Ageing Res. Rev.* **24**, 77–82 (2015).
7. Courties, G. et al. Ischemic stroke activates hematopoietic bone marrow stem cells. *Circ. Res.* **116**, 407–417 (2015).
8. Morrison, S. J. & Scadden, D. T. The bone marrow niche for haematopoietic stem cells. *Nature* **505**, 327–334 (2014).
9. Itkin, T. et al. Distinct bone marrow blood vessels differentially regulate haematopoiesis. *Nature* **532**, 323–328 (2016).
10. Gamache, D. A., Povlishock, J. T. & Ellis, E. F. Carrageenan-induced brain inflammation. Characterization of the model. *J. Neurosurg.* **65**, 679–685 (1986).
11. Ueda, Y., Kondo, M. & Kelsoe, G. Inflammation and the reciprocal production of granulocytes and lymphocytes in bone marrow. *J. Exp. Med.* **201**, 1771–1780 (2005).
12. Hill, W. D. et al. SDF-1 (CXCL12) is upregulated in the ischemic penumbra following stroke: association with bone marrow cell homing to injury. *J. Neuropathol. Exp. Neurol.* **63**, 84–96 (2004).
13. Heidt, T. et al. Chronic variable stress activates hematopoietic stem cells. *Nat. Med.* **20**, 754–758 (2014).
14. Zenker, W. & Kubik, S. Brain cooling in humans–anatomical considerations. *Anat. Embryol. (Berl.)* **193**, 1–13 (1996).
15. Adeeb, N., Mortazavi, M. M., Tubbs, R. S. & Cohen-Gadol, A. A. The cranial dura mater: a review of its history, embryology, and anatomy. *Childs Nerv. Syst.* **28**, 827–837 (2012).
16. Hershkovitz, I. et al. The elusive diploic veins: anthropological and anatomical perspective. *Am. J. Phys. Anthropol.* **108**, 345–358 (1999).
17. Rangel de Lázaro, G., de la Cuétara, J. M., Píšová, H., Lorenzo, C. & Bruner, E. Diploic vessels and computed tomography: segmentation and comparison in modern humans and fossil hominids. *Am. J. Phys. Anthropol.* **159**, 313–324 (2016).
18. Lucchinetti, C. F. et al. Inflammatory cortical demyelination in early multiple sclerosis. *N. Engl. J. Med.* **365**, 2188–2197 (2011).
19. Michaud, J. P., Bellavance, M. A., Préfontaine, P. & Rivest, S. Real-time in vivo imaging reveals the ability of monocytes to clear vascular amyloid beta. *Cell Rep.* **5**, 646–653 (2013).
20. Prokop, S. et al. Impact of peripheral myeloid cells on amyloid-β pathology in Alzheimer's disease-like mice. *J. Exp. Med.* **212**, 1811–1818 (2015).
21. Zenaro, E. et al. Neutrophils promote Alzheimer's disease-like pathology and cognitive decline via LFA-1 integrin. *Nat. Med.* **21**, 880–886 (2015).
22. Park, L. et al. Brain perivascular macrophages initiate the neurovascular dysfunction of Alzheimer Aβ peptides. *Circ. Res.* **121**, 258–269 (2017).
23. Faraco, G., Park, L., Anrather, J. & Iadecola, C. Brain perivascular macrophages: characterization and functional roles in health and disease. *J. Mol. Med. (Berl.)* **95**, 1143–1152 (2017).
24. Abtin, A. et al. Perivascular macrophages mediate neutrophil recruitment during bacterial skin infection. *Nat. Immunol.* **15**, 45–53 (2014).
25. Perez-de-Puig, I. et al. Neutrophil recruitment to the brain in mouse and human ischemic stroke. *Acta Neuropathol.* **129**, 239–257 (2015).
26. Bartholomäus, I. et al. Effector T cell interactions with meningeal vascular structures in nascent autoimmune CNS lesions. *Nature* **462**, 94–98 (2009).
27. Coles, J. A., Myburgh, E., Brewer, J. M. & McMenamin, P. G. Where are we? The anatomy of the murine cortical meninges revisited for intravital imaging,

immunology, and clearance of waste from the brain. *Prog. Neurobiol.* **156**, 107–148 (2017).
28. Louveau, A. et al. Structural and functional features of central nervous system lymphatic vessels. *Nature* **523**, 337–341 (2015).
29. Aspelund, A. et al. A dural lymphatic vascular system that drains brain interstitial fluid and macromolecules. *J. Exp. Med.* **212**, 991–999 (2015).
30. McKittrick, C. M., Lawrence, C. E. & Carswell, H. V. Mast cells promote blood brain barrier breakdown and neutrophil infiltration in a mouse model of focal cerebral ischemia. *J. Cereb. Blood Flow Metab.* **35**, 638–647 (2015).
31. Arac, A. et al. Evidence that meningeal mast cells can worsen stroke pathology in mice. *Am. J. Pathol.* **184**, 2493–2504 (2014).
32. Sellner, J. & Leib, S. L. In bacterial meningitis cortical brain damage is associated with changes in parenchymal MMP-9/TIMP-1 ratio and increased collagen type IV degradation. *Neurobiol. Dis.* **21**, 647–656 (2006).
33. Kruger, P. et al. Neutrophils: between host defence, immune modulation, and tissue injury. *PLoS Pathog.* **11**, e1004651 (2015).
34. Shi, Y., Leak, R. K., Keep, R. F. & Chen, J. Translational stroke research on blood-brain barrier damage: challenges, perspectives, and goals. *Transl. Stroke Res.* **7**, 89–92 (2016).

Acknowledgements

The authors thank M. Ericsson (HMS Electron Microscopy Facility) for skull sample preparation, sectioning, and assistance with EM imaging. We acknowledge D. Capen (Center for Systems Biology and Program in Membrane Biology/Division of Nephrology, MGH) for help with interpretation of electron microscopy data. The authors thank the MGH mouse imaging program and the Center for Skeletal Research Core (NIH P30 AR066261) for assistance with imaging. This work was funded in part by grants from the National Institutes of Health (NS084863 and HL139598), the American Heart Association (16SDG30190009), the Cure Alzheimer's Fund, the Global Research Lab (GRL) program (NRF-2015K1A1A2028228) of the National Research Foundation by the Korean government, and by fellowships from the Netherlands Organisation for Scientific Research (NWO, Rubicon Grant: 835.15.014), the Deutsche Forschungsgemeinschaft (RO5071/1-1), and the MGH Research Scholar program.

Author contributions

F.H. conceived the study, designed, performed, and analyzed most experiments and contributed to writing the manuscript. V.F., G.C., D.R., Y.S., K.V., G.R.W., J. K., C.V., and G.S.M. performed flow cytometry and imaging experiments. D.E.K., R.W., F.K.S., and M.A.M. discussed and interpreted data, provided strategic input, raised funding, and edited the manuscript. M.N. supervised the study and wrote the manuscript with input from all authors.

Competing interests

The authors declare no competing interests.

Additional information

Supplementary information is available for this paper at https://doi.org/10.1038/s41593-018-0213-2.

Reprints and permissions information is available at www.nature.com/reprints.

Correspondence and requests for materials should be addressed to M.N.

Publisher's note: Springer Nature remains neutral with regard to jurisdictional claims in published maps and institutional affiliations.

Methods

Animals and experimental parameters. We used 4-week-old and 3-month-old male C57BL/6 mice from Jackson Laboratories, and bred heterozygous Cx3cr1^{GFP} (3- to 6-month-old males were used in experiments). All the procedures were performed in accordance with the ARRIVE guidelines and the *Guide for Care and Use of Laboratory Animals* (NIH Publication No. 85-23, 1996), and have been approved by the institutional review board (MGH Subcommittee on Research Animal Care). Mice were randomly distributed to experimental groups. As the same experimenter performed the surgeries, organ and sample harvesting, and sample preparation for flow cytometry, blinding was not implemented.

Human samples. The Institutional Review Board of Dongguk University at the Ilsan Hospital approved this study. All patients or their legally authorized representatives gave written informed consent. We imaged skull specimens obtained from two males (52 and 33 year old) and one female (53 years old). The 52-year-old male had decompression surgery 2 d after bilateral ischemic stroke, and his comorbidities were hyperlipidemia, hypertension, and diabetes mellitus. The other male had decompression surgery after trauma. The female patient underwent retromastoid craniotomy for microvascular decompression surgery.

Bone marrow tagging by microinjection technique. Deep red CellTracker (C34565 Molecular Probes) and CMFDA (green) CellTracker (C7025 Molecular Probes) dyes were prepared fresh before each experiment by dissolving them in 3 µL DMSO (D8418 Sigma) and then adding 297 µL sterile saline. Microinjection of the tibia and skull marrow were performed sequentially under 1.5% isoflurane anesthesia, using a 5-µL syringe (#65 Hamilton Co, Reno, NV USA) mounted with a custom 34-gauge blunt needle (RN 0.375" PT3). Aseptic technique was used for each procedure. The skin above the skull was opened at the midline to expose both anterior (near bregma) and posterior (beside the cerebellum) marrow sites. One or two microinjections were performed for each marrow site (right frontal, left frontal, and occipital). First, 'predrilling' was done using a 30-gauge needle (ref #305106 BD) with great care to prevent perforation of the inner wall of the skull. Animals with unsuccessful procedures at this stage were removed from the study. A total volume of about 2–3 µL of the red tracker was slowly injected per injection site through the predrilled spots (20–30 s per injection), for a total of 10 µL of red tracker injected per skull (4 injection sites). The injection was monitored through the microscope. Thereafter, the skin was sutured with 6-0 silk. The skull was kept moist throughout the procedure using sterile saline. For the tibia marrow injection, disinfected skin was opened just below the knee and the muscle insertion locally scrapped off the bone at the chosen injection site. The bone wall was perforated with a 30-gauge needle (ref # 305106 BD). The needle of the Hamilton syringe was introduced into the marrow cavity to inject 3 µL of the green cell tracker over 30 s. The skin was sutured with 6-0 thread. Animals were killed for analysis 6–48 h after injection, followed by cardiac perfusion with 20 mL of PBS.

Stroke induction. Stroke was induced using a filament MCAO (middle cerebral artery occlusion) model under anesthesia (1.5% isoflurane) and using a temperature-control system (Harvard apparatus, Holliston, MA USA). Mice were given preemptive analgesia (buprenorphine 0.1 mg/kg SC) and follow-up doses until they were killed for analysis. Briefly, the right carotid bifurcation was accessed through cervicotomy and careful dissection. After permanent ligation of the external carotid artery (ECA), a silicon coated 7-0 filament (Doccol corporation, Sharon, MA USA) was introduced from the ECA to the internal carotid artery until block. The filament was left in place either permanently or for 30 min and then pulled out to achieve reperfusion. Success of the procedure was monitored by the presence of a brain cortical pallor/edema at death, or the presence of neurological signs on basic mouse examination (circling behavior, impaired forelimb flexion associated with clasping reflex). Corresponding sham surgery comprised skin-opening, dissection of the carotid bifurcation, and ligation of the right external carotid artery.

Carrageenan injection. For intracisternal (IC) injections, pre-emptive buprenorphine (Buprenex) was given subcutaneously (0.1 mg/kg). Lambda carrageenan was bought from Sigma (#22049). To induce aseptic meningoencephalitis, we adapted a published protocol[10] and injected 5 µL of 0.5% carrageenan (w/V) diluted in sterile saline in the cisterna magna, during 1.5% isoflurane anesthesia. The mouse was installed on a stereotactic frame (Stoelting, Wood dale IL USA). After shaving, disinfection, opening of the skin, and dissection of the cervical muscles, the cisterna magna membrane was visualized under microscopy and punctured using a Hamilton syringe (Gastight #1701) mounted with a 34-gauge needle. Carrageenan was injected slowly over 1 min. Excess carrageenan was removed with a cotton swab. The skin was then sutured and the mouse allowed to recover. Corresponding sham surgery consisted of skin opening and dissection of the cervical muscles only.

Myocardial infarction. Under isoflurane anesthesia, the mouse was intubated and ventilated (Inspira, Harvard Apparatus). A thoracotomy was then performed between the third and fourth ribs to visualize the heart. After removing the connective tissue, an 8-0 suture was placed to ligate the left coronary artery. The rib cage was then closed with two separate 5-0 sutures, a 20-gauge sheath left between the sutures, and the dermis glued shut with surgical glue. Finally, air was removed from the thoracic cavity via the sheath and a 3-mL syringe before the animal was extubated.

Confocal microscopy. Microscopy of the skull, tibia, or brain was performed with a confocal microscope (IV100 Olympus). Field of view at 4× magnification covers 2,290 µm by 2,290 µm, and at 20× covers 458 µm by 458 µm with a resolution of 512 by 512 pixels. For video acquisition, time-lapse was either 1.64 or 4.89 s per image. Images were reconstructed using Imaris software (Bitplane, Zurich, Switzerland) or Matlab. For in vivo imaging, we used a customized Olympus FV1000 BX61-W1 (Olympus America) confocal/multiphoton microscope. A 20× water-immersion objective with a high numerical aperture (NA) and large working distance (Olympus, XLUMPLFLN 1 NA, 2-mm wd) were used for imaging. Images 256×256 in size and with 4 µs/pixel integration time were acquired in confocal modality.

Histology. After the mice were killed with cardiac perfusion of 20 mL PBS, brains were frozen at −35 °C in 2-methyl-butane and further sectioned at 50 µm on a cryostat (CM 3050 S, Leica, Wetzlar, Germany). After postfixation in 4% paraformaldehyde, the sections were imaged on a microscope (Eclipse TE2000-U Nikon).

Electron microscopy. Tissues were fixed by cardiac perfusion with formaldehyde/glutaraldehyde (2.5% each) followed by postfixation overnight in the same fixative. Calvaria were decalcified with 4.13% EDTA and 0.44% NaOH in distilled water (pH 7.3) at 4 °C with solution changed every 2 d for at least 2 weeks. The samples were then washed in 0.1 M cacodylate buffer and postfixed with 1% osmium tetroxide (OsO_4)/1.5% potassium-ferrocyanide ($KFeCN_6$) for 1 h, washed in water 3 times, and incubated in 1% aqueous uranyl acetate for 1 h, followed by two washes in water and then dehydration in ethanol. The samples were then put in propylene oxide for 1 h and incubated overnight in a 1:1 mixture of propylene oxide and TAAB Epon (Marivac Canada Inc. St. Laurent, Canada). The following day the samples were embedded in TAAB Epon and polymerized at 60 °C for 48 h. Ultrathin 80-nm-thick sections were cut on a Reichert Ultracut-S microtome, placed on copper grids, stained with lead citrate, and examined in a JEOL 1200EX transmission electron microscope. Images were recorded with an AMT 2k CCD camera.

Ex vivo microscopy of the skull and the tibia. To identify bone, animals were injected with Osteosense 750EX (4 nmol/mouse, PerkinElmer) the day before imaging. The vasculature was labeled in vivo with 50 µL of RPE anti-mouse CD31 antibody (#553373, BD Biosciences) or isolectin B4 (FL-1201, Vector Labs), injected IV 1 h before the mouse was killed. Mice were killed 2 h after either skull or tibia microinjection by perfusion with 20 mL of PBS or 7 h after systemic injection of Evans Blue 3% (w/vol in sterile saline). The skull and tibiae were dissected and cleaned before fixation for 1 h in 4% paraformaldehyde in PBS, then rinsed twice in PBS for 10 min. Tibiae were then embedded in Tissue-Tek O.C.T (#4583, Sakura Finetek Inc., Torrance, CA, USA) on dry ice and kept at −20 °C. They were later shaved on a cryostat (CM 3050 S, Leica, Wetzlar, Germany) to expose the bone marrow compartment. *Z*-stack images were acquired with 2-µm steps at 20× magnification. Images were processed using Imaris (Bitplane, Zurich, Switzerland). Maps of the entire bones for the injection sites were generated by stitching together multiple images acquired at 4× magnification, using the Affinity Designer software (Serif, Nottingham, UK). Sizes of the channels were determined manually using the measuring distance tool in Imaris (Bitplane, Zurich, Switzerland).

Skull marrow organ bath. To explore cell traffic through the skull channels to the meninges, we employed an organ bath system. After in vivo staining of the bone surface with Osteosense 750EX (4 nmol/mouse, PerkinElmer) the day before the experiment, the vasculature and neutrophils were stained with IV injections of 50 µL of RPE anti-mouse CD31 (#553373, BD Biosciences) and 50 µL of APC anti-mouse Ly6G (#127614, Biolegends) antibodies 1 h before the mice were killed. Using surgical scissors, we obtained a skull piece of about 4 by 4 mm, respecting the integrity of the dura and the visible edges of the marrow cavities. This specimen was flipped upside down and rapidly transferred into the organ bath. The specimen was placed on a stage and immersed in a solution of 50 µmol fMLP (F3506 Sigma-Aldrich), used as chemoattractant, in HBSS. This protocol was adopted from previously published in vitro neutrophil migration assays[35]. The organ bath was maintained at 37 °C by a warming plate (ATC-2000 World Precision Instruments). The same conditions were implemented to explore neutrophil migration through the channels 4–6 h after permanent MCAO or after intracisternal injection of carrageenan, and corresponding sham or naive controls. Neutrophils exiting the channels were identified and counted using Imaris (Bitplane).

Flow cytometry. To study the skull bone marrow, the entire calvarium and the sphenoid bone were harvested. The dura was removed using a microscope. Cell suspension was prepared by mincing the calvarium and sphenoid for 2.5 min in

buffer (2.5% albumin in PBS). The obtained suspension was then filtered through a 40-µm cell strainer into a 50-mL Falcon tube. The marrow from long bones was collected by flushing. Spine bone marrow was obtained by crushing. Marrow from sternum and pelvis bones was also obtained by crushing. Enumeration of bone marrow cellularity for all bones in naive mice relied on bones prepared by crushing only. After centrifugation at 340 *g* for 7 min at 4 °C, samples were resuspended in 300 µL of buffer and kept at 4 °C until staining.

Either one (stroke hemisphere) or both hemispheres (carrageenan) were collected and weighted for analysis[36]. Samples were digested for 20 min at 37 °C in 5 mL of HBSS containing 10% fetal bovine serum (#16140071, Gibco) and 1% (w/V) collagenase (#C5138, Sigma). After homogenization, samples were passed through a 40-µm mesh cell strainer to a 50-mL Falcon tube. The suspension was completed to 30 mL with PBS and centrifuged at 450 *g* for 5 min. The remaining pellet was suspended in 10.5 mL of PBS and gently homogenized with 4.5 mL of isotonic Percoll (GE Healthcare). The myeloid layer was collected by aspiration after 35 min of centrifugation (900 *g*) with no brake at 4 °C. The Percoll was then washed off and cells were finally resuspended in 300 µL of PBS after a last centrifugation (450 *g*, 5 min). Hearts were digested using a mixture of collagenase I (450 U/mL, #C0130 Sigma), collagenase XI (125 U/mL, #C7657 Sigma), hyaluronidase (60 U/mL, #H3605 Sigma), DNAse I (60 U/mL, #D5319, Sigma), and HEPES buffer (20 µM) in PBS at 37 °C for 1 h under gentle shaking at 750 rpm. After homogenization, the preparation was filtered, washed off in buffer, spun, and resuspended in PBS. Blood was collected by retro-orbital bleeding under anesthesia at the time the mice were killed. Spleens were immediately mashed through a 40-µm mesh on top of a 50-mL Falcon tube and suspended in 15–20 mL of buffer. After a first centrifugation (340 *g*, 7 min, 4 °C), hypotonic red blood cell (RBC) lysis was performed for both the blood and the spleen (#420301, Biolegends). Samples were centrifuged again (340 *g*, 7 min, 4 °C) before resuspension in 300 µL (blood) or 1 mL (spleen) FACS buffer (PBS with 0.5% bovine serum albumin). The total number of cells per sample was determined using a hemocytometer and Trypan Blue staining for cell viability (Cellgro, Mediatech Inc., VA, USA). For cellularity in all bone marrow compartments in naive mice, automated cell counting was used (Countess, ThermoFisher). Leucocyte staining was performed at 4 °C for 20 min, using a combination of antibodies at a concentration of 1:300. Viability was assessed using a live/dead dye (L-34966, Life Technologies). After staining samples, were fixed (BD Cytofix, 10 min on ice). The list of antibodies used for the experiments is provided in Supplementary Table 1.

Samples were recorded on a LSRII Flow Cytometer (BD) and data were analyzed with FlowJo software (Tree Star). Cell numbers per sample were calculated as total cells per sample multiplied by the percentage of live cells obtained from the appropriate flow cytometry gate. After gating out the lineage-positive cells (Ter119, c-kit, CD11c, CD3, CD90, NK 1.1, CD31, and B220), mature myeloid cells were identified as $CD45^+$ and $CD11B^+$. Subpopulations of myeloid cells were defined as follows: neutrophils ($Ly6G^+$ and $CD115^-$), Ly6Chi monocytes ($CD115^+$ $Ly6C^+$), and microglia ($Ly6G^-$ and $Ly6C^-$).

For the experiments involving bone marrow tagging, Deep red CellTracker and CMFDA (green) CellTracker were analyzed in the APC and FITC channels according to the excitation/emission peaks provided by the manufacturer (492/517 nm and 630/660 nm, respectively). The neutrophil population was analyzed for the presence of cells positive for the trackers at high fluorescence intensity. To take into account both potential autofluorescence and unspecific staining by the dyes at lower fluorescence intensity from circulation, the gate position for each cell tracker was based on animals that were injected IV with the same dose.

In vitro fluorescence assay for red and green trackers. Deep red CellTracker (C34565, Molecular Probes) and CMFDA (green) CellTracker (C7025, Molecular Probes) dyes were prepared fresh by dissolution in 3 µL DMSO (D8418 Sigma) in 297 µL FACS buffer (PBS with 0.5% bovine serum albumin) or serum (FBS #16140071, Gibco). A cell suspension was obtained from flushed tibiae as described above. A total of 700,000 cells were incubated with either the green or the red cell tracker at different concentration levels for 15 min at room temperature (20–25 °C). Cells were then washed and resuspended in FACS buffer for flow cytometry.

Measurement of SDF-1 in bone marrow serum by ELISA. Murine SDF-1 was quantified by an ELISA kit (DY460 Duoset). Tibial (sectioned in half) and skull (minced in PBS) marrow serum was obtained after centrifugation in a custom-made two-compartment system (11,750 *g*, 3 min). The supernatant was used as indicated by the manufacturer's instructions.

In vivo bone marrow permeability to Evans Blue dye. The protocol was adapted from Itkin et al.[9]. Evans Blue 3% (w/vol in sterile saline) was injected via the jugular vein at the time of reperfusion in stroke mice (30-min occlusion time) or immediately after intracisternal injection of carrageenan at a dose of 0.07 mg/g of body weight. The entire calvarium, the sphenoid bone, and both tibia were harvested. The periosteum and dura attached to the skull samples were removed under microscopy. The pieces were then minced in 200 µL formamide for 2 min. The tibiae were individually spun dry in a custom-made two-compartment system at 11,750 *g* for 3 min to recover all marrow, which was homogenized in 200 µL formamide by vortexing. Evans Blue extraction was realized overnight at 60 °C and 700-rpm shaking. After centrifugation at 2,000 *g* for 30 min, 50 µL of the supernatant was plated and read for absorbance by dual-wavelength spectrophotometric analysis at 620 nm and 740 nm (Tecan, Switzerland). Standards were prepared with Evans Blue diluted in formamide (0 to 250 µg/mL). Absorbance was corrected for potential hematic contamination, as previously published[9], using the formula: corrected absorbance at 620 nm = actual absorbance at 620 nm – (1.426 × (absorbance at 740 nm) + 0.03). Values were then subtracted for blank and Evans Blue amount calculated from the standards.

Mouse neutrophil transmigration assay. Mouse brain endothelial cells (MBEC) were obtained from Cell Biologics (C57-6023) and cultured on polyethylene collagen-coated membranes (8-µm pore size; Falcon, 353182) in supplemented EBM-2 media (Lonza) until confluence. Neutrophils were isolated from skull and tibia bone marrow on MACS columns after staining with the manufacturer's antibody mix (negative selection, Miltenyi, 130097658) from 6 wild-type 3-month-old C57BL/6 mice. Cells originating from skull and tibia from the same mouse were loaded with red (skull) and green (tibia) cell-trackers, respectively, for 3 animals, and green (skull) and red (tibia) cell-trackers for the 3 others, in accordance with manufacturer's instructions (deep red CellTracker, C34565, Molecular Probes; and CMFDA (green) CellTracker, C7025, Molecular Probes). Cells were counted to obtain a cell suspension of 50% skull and 50% tibial origin.

Prior to the transmigration assay, MBECs were activated with TNFα (10 ng/mL) for 8 h and then washed. Neutrophil attractant fMLP was used at a concentration of 50 µmol to facilitate migration toward the bottom part of the well. Finally, cells (200,000 from each compartment) were deposited on the upper part of the transwell. After 2 h, the number of cells that had migrated through the membrane was counted manually, and the composition of the population assessed by flow cytometry. The percentage of migrated cell was calculated as follows: (migrated number of cells)/(initial number of cells above the membrane).

High-resolution X-ray computed tomography. Calvaria and sphenoid bone were dissected in a naive 3-month-old C57BL/6 mouse after it was killed for analysis. Ex vivo human occipital bone, mouse frontal bone, and mouse tibial samples were scanned on a high-resolution CT scanner (µCT40, Scanco Medical AG, Brüttisellen, Switzerland). Data were acquired using a 6-μm^3 isotropic voxel size, 70-kVp peak X-ray tube intensity, 114-µA X-ray tube current, and 200-ms integration time, and they were subjected to Gaussian filtration. Images were generated with Horos (https://www.horosproject.org) and Osirix (Pixmeo, Bernex, Switzerland). Image renderings were performed in Amira (FEI, Hillsboro, OR).

The human skull samples were imaged, as previously reported[37], using microCT (mCT, NFR Polaris-G90; NanoFocusRay, Jeonju, Korea): 65 kVp, 60 µA, 500 ms per frame, 360 views, 512 × 512 reconstruction matrix, 600 slices. The data were converted to the Digital Imaging and Communications in Medicine format (Lucion; MeviSYS, Seoul, Korea).

The human and mouse skull bone CTs were segmented by thresholding using Amira. Channel size was determined by segmenting voxels that were 3 s.d. below the mean table Hounsfield units. Channel diameters were manually determined by measuring the maximum diameter of individual channels below a Hounsfield threshold, which was 3 s.d. below that of the cortical bone's mean. Mouse tibiae were analyzed in similar fashion by removing the trabecular bone to isolate the cortical bone of an 0.15-cm axial section along the tibial crest. 3D image visualization was performed in Amira.

Statistics. We used GraphPad Prism 7 (GraphPad Inc.) for statistical analyses. Results are reported as mean ± s.e.m. For group comparisons, two-tailed nonparametric Mann–Whitney tests, Welch's *t* tests, or paired Wilcoxon tests were executed. For comparing more than two groups, a nonparametric Kruskal–Wallis test was applied. P values < 0.05 indicated statistical significance. No statistical methods were used to predetermine sample sizes[7,13]. Data distribution was assumed to be normal, but this was not formally tested. There was no formal randomization. Data collection and analysis were not performed blind to the conditions of the experiments.

Reporting Summary. Further information on experimental design is available in the Nature Research Reporting Summary linked to this article.

Data availability. The data that support the findings of this study are available from the corresponding authors upon reasonable request.

References

35. Keenan, T. M. & Folch, A. Biomolecular gradients in cell culture systems. *Lab Chip* **8**, 34–57 (2008).
36. Lelios, I. & Greter, M. Isolation of leukocytes from mouse central nervous system. *Methods Mol. Biol.* **1193**, 15–19 (2014).
37. Kim, J. Y. et al. Direct imaging of cerebral thromboemboli using computed tomography and fibrin-targeted gold nanoparticles. *Theranostics* **5**, 1098–1114(2015).

nature research

Corresponding author(s): Nahrendorf

Reporting Summary

Nature Research wishes to improve the reproducibility of the work that we publish. This form provides structure for consistency and transparency in reporting. For further information on Nature Research policies, see Authors & Referees and the Editorial Policy Checklist.

Statistical parameters

When statistical analyses are reported, confirm that the following items are present in the relevant location (e.g. figure legend, table legend, main text, or Methods section).

n/a	Confirmed	
☐	☒	The exact sample size (*n*) for each experimental group/condition, given as a discrete number and unit of measurement
☐	☒	An indication of whether measurements were taken from distinct samples or whether the same sample was measured repeatedly
☐	☒	The statistical test(s) used AND whether they are one- or two-sided *Only common tests should be described solely by name; describe more complex techniques in the Methods section.*
☒	☐	A description of all covariates tested
☒	☐	A description of any assumptions or corrections, such as tests of normality and adjustment for multiple comparisons
☐	☒	A full description of the statistics including central tendency (e.g. means) or other basic estimates (e.g. regression coefficient) AND variation (e.g. standard deviation) or associated estimates of uncertainty (e.g. confidence intervals)
☐	☒	For null hypothesis testing, the test statistic (e.g. *F*, *t*, *r*) with confidence intervals, effect sizes, degrees of freedom and *P* value noted *Give P values as exact values whenever suitable.*
☒	☐	For Bayesian analysis, information on the choice of priors and Markov chain Monte Carlo settings
☒	☐	For hierarchical and complex designs, identification of the appropriate level for tests and full reporting of outcomes
☒	☐	Estimates of effect sizes (e.g. Cohen's *d*, Pearson's *r*), indicating how they were calculated
☐	☒	Clearly defined error bars *State explicitly what error bars represent (e.g. SD, SE, CI)*

Our web collection on statistics for biologists may be useful.

Software and code

Policy information about availability of computer code

Data collection	Imaris (version 7.7.2) or Matlab (version R2015a) softwares were use to reconstruct images. Affinity designer (version 1.6.1) software was used to stich 4X images for microscopy. MicroCT images were generated with Horos (version 1.1.7, https://www.horosproject.org) and Osirix software (version 3.8.1). MicroCT image renderings were performed in the Amira software (version 5.3) environment. FlowJo software (version X 10.0.7r2) was use to generate flow cytometry dotplots.
Data analysis	Imaris software (version 7.7.2) was used to analyze images. FlowJo sofware (X 10.0.7r2) was used to anayze flow cytometry data. Statistical analyses were performed using Graphpad Prism 7 software.

For manuscripts utilizing custom algorithms or software that are central to the research but not yet described in published literature, software must be made available to editors/reviewers upon request. We strongly encourage code deposition in a community repository (e.g. GitHub). See the Nature Research guidelines for submitting code & software for further information.

Data

Policy information about availability of data

All manuscripts must include a data availability statement. This statement should provide the following information, where applicable:

- Accession codes, unique identifiers, or web links for publicly available datasets
- A list of figures that have associated raw data
- A description of any restrictions on data availability

The data that support the findings of this study are available from the corresponding authors upon reasonable request.

Field-specific reporting

Please select the best fit for your research. If you are not sure, read the appropriate sections before making your selection.

☒ Life sciences ☐ Behavioural & social sciences ☐ Ecological, evolutionary & environmental sciences

For a reference copy of the document with all sections, see nature.com/authors/policies/ReportingSummary-flat.pdf

Life sciences study design

All studies must disclose on these points even when the disclosure is negative.

Sample size	Sample sizes were chosen based on prior imaging and flow cytometry data. No statistical predetermination of sample size was done.
Data exclusions	No data were excluded.
Replication	All experiments were done in duplicate the least unless specified otherwise. Certain experiments were done only once: costly experiments (e.g. electron microscopy, microCT), pilot experiments for technical optimization of the micro-injection technique (cell tracker titration, sub-dural cell tracker injection), or experiments performed for illustrative purpose (e.g. 1d).
Randomization	Mice were randomly allocated to experimental groups. There are no treatment studies in this manuscript.
Blinding	The investigator was not blinded to group allocation as this was obvious during the experiments (e.g. stroke vs sham).

Reporting for specific materials, systems and methods

Materials & experimental systems

n/a	Involved in the study
☒	☐ Unique biological materials
☐	☒ Antibodies
☒	☐ Eukaryotic cell lines
☒	☐ Palaeontology
☐	☒ Animals and other organisms
☐	☒ Human research participants

Methods

n/a	Involved in the study
☒	☐ ChIP-seq
☐	☒ Flow cytometry
☒	☐ MRI-based neuroimaging

Antibodies

Antibodies used	Commercially available antibodies were used and are described appropriately in the method section and Supplemental Table 1.
Validation	Antibodies were commercially available and validated by the vendors.

Animals and other organisms

Policy information about studies involving animals; ARRIVE guidelines recommended for reporting animal research

Laboratory animals	We used 4 week and 3 month old male C57BL/6 from Jackson laboratories, and bred heterozygous Cx3cr1GFP (3-6 month old males were used in experiments).

Wild animals	None
Field-collected samples	None

Human research participants

Policy information about studies involving human research participants

Population characteristics	Three patients that underwent cranial surgery were consented to provide a specimen. These were the three first available skull specimen available during the revision period.
Recruitment	The first three consecutively available patients undergoing craniotomy, that consented to participate, were recruited to investigate if skull channels are present in humans. There were no exclusion criteria.

Flow Cytometry

Plots

Confirm that:

☒ The axis labels state the marker and fluorochrome used (e.g. CD4-FITC).

☒ The axis scales are clearly visible. Include numbers along axes only for bottom left plot of group (a 'group' is an analysis of identical markers).

☒ All plots are contour plots with outliers or pseudocolor plots.

☒ A numerical value for number of cells or percentage (with statistics) is provided.

Methodology

Sample preparation	Brain and tissue samples from mice were prepared by digestion, washing and staining as previously described and as listed in the method section.
Instrument	LSR2 flow cytometer
Software	Vendor software from BD
Cell population abundance	No cell sorting was done. All analyzed cell populations were abundant enough for analysis.
Gating strategy	The entire gating strategy is reported in supplemental data, and the appropriate staining controls for proper gate placements.

☒ Tick this box to confirm that a figure exemplifying the gating strategy is provided in the Supplementary Information.